Batteries & Supercaps

Research Article
doi.org/10.1002/batt.202300101

Chemistry Europe
European Chemical
Societies Publishing

www.batteries-supercaps.org

Special Collection

Ionothermally Synthesized Nanoporous Ti$_{0.95}$W$_{0.05}$Nb$_2$O$_7$: a Novel Anode Material for High-Performance Lithium-Ion Batteries

Runming Tao[+, a, b, c] Tianyu Zhang[+, a] Xiao-Guang Sun,[b] Chi-Linh Do-Thanh,[a] and Sheng Dai*[a, b]

Although TiNb$_2$O$_7$ is regarded as a fast-rechargeable lithium-ion battery (LIB) anode material, the intrinsic poor electrochemical kinetics of TiNb$_2$O$_7$ still dramatically impedes its development. Herein, an ionothermal synthesis-assisted doping strategy is proposed for the preparation of a new W^{6+}-doped TiNb$_2$O$_7$ material (Ti$_{0.95}$W$_{0.05}$Nb$_2$O$_7$) with nanoporous structure (denoted as NPTWNO). The improved Li$^+$ diffusion coefficient of NPTWNO suggests that the ionic-liquid-templated nanoporous architecture improves the Li$^+$ diffusion kinetics. The density functional theory computational study reveals that the doped W^{6+} successfully boosts the electronic conductivity due to the narrowed conduction-valance bandgap resulted from charge redistribution, which is reflected by the electrochemical impedance spectroscopy data. With the simultaneously enhanced Li$^+$ diffusivity and electronic conductivity, NPTWNO achieves fast-rechargeability in LIBs. Therefore, this work indicates the potential of ionothermal synthesis-assisted doping strategy on energy storage materials and offers NPTWNO material with promising electrochemical performance.

Introduction

During the past decades, lithium-ion batteries (LIBs) have been increasingly employed in electric vehicles (EVs) as the power sources due to the global warming concern of the CO$_2$ emission from gas-powered vehicles.[1] Unfortunately, the broadly used graphite-based LIBs cannot fulfill the requirement of high-rate charging. Graphite's low operation potential (0.1 V vs. Li/Li$^+$) with the generation of passivating solid-electrolyte interphase (SEI) dramatically impedes its future application in EVs due to the unsafe Li-plating during high rate charging.[2] Spinel Li$_4$Ti$_5$O$_{12}$ (LTO) with a high working potential of 1.55 V vs. Li/Li$^+$ and zero-strain property has been proposed as an excellent anode material for fast-charging, but its low specific capacity (175 mAh g^{-1}) cannot fit the crucial needs of large-scale energy storage.[3]

[a] Dr. R. Tao,$^+$ Dr. T. Zhang,$^+$ Dr. C.-L. Do-Thanh, Prof. S. Dai
Department of Chemistry, Institute for Advanced Materials and Manu-
facturing
The University of Tennessee, Knoxville
Knoxville, Tennessee 37996 (USA)
E-mail: dais@ornl.gov

[b] Dr. R. Tao,$^+$ Dr. X.-G. Sun, Prof. S. Dai
Chemical Sciences Division
Oak Ridge National Laboratory
Oak Ridge, Tennessee 37830 (USA)

[c] Dr. R. Tao$^+$
Electrification and Energy Infrastructures Division
Oak Ridge National Laboratory
Oak Ridge, Tennessee 37831 (USA)

[+] These authors contributed equally to this work.

💻 Supporting information for this article is available on the WWW under https://doi.org/10.1002/batt.202300101

Special Collection An invited contribution to a Special Collection on Fast Charging Batteries

A few years ago, Goodenough et al. proposed TiNb$_2$O$_7$ (TNO) as a promising candidate to substitute for LTO.[4] Because TNO with a safe operation voltage of 1.66 V vs Li/Li$^+$ and three redox couples Ti^{4+}/Ti^{3+}, Nb^{5+}/Nb^{4+} and Nb^{4+}/Nb^{3+} can deliver a higher specific capacity (388 mAh g^{-1}) than graphite (372 mAh g^{-1}) and LTO do.[2b,3b] However, similar to other metal oxides, the intrinsically low ionic diffusivity and poor electronic conductivity restrict the commercial applications of TNO materials.[2b,3a,b,4a] One strategy to address the limit of ionic diffusivity is to reduce the particle size based on the correlation of $\tau \sim L^2/D$, where τ represents the Li$^+$ diffusion time, L means the diffusion length, and D indicates the diffusion coefficient for Li$^+$ in the solid.[2b,5] Another strategy is to introduce porosity into the active material to enhance the contact between electrode and electrolytes.[2b] For instance, our group once applied ionic liquids (ILs) in the synthesis of multiple materials, such as porous carbonaceous and metal oxides.[6] Recently, we have combined those two strategies together to synthesize a nanoporous TNO material with superior electrochemical properties by applying an IL as the template based on the intermolecular interactions of IL, including the anions-precursors hydrogen bonding effects and the neighboring imidazolium rings' π–π stack interactions, which thereby enhances the Li$^+$ diffusivity.[7] On the other hand, an effective method to overcome the disadvantage of electronic conductivity is to dope, high valence transition metal cations doping due to the bandgap reduction of the material's conduction-valence bands by the impurity band formation.[4a,8] For example, although a few groups previously used mechanochemical approach to develop doped TNO materials,[4a,8a,9] the large and unfavorable particle sizes of products could not be avoided. So far, to the best of our knowledge, limited work has been done to combine

those pre-mentioned strategies to resolve the fundamental disadvantages of TNO material.

Herein, we report a novel type of tungsten doped nanoporous $TiNb_2O_7$ material by ionothermal synthesis. The obtained nanoporous $Ti_{0.95}W_{0.05}Nb_2O_7$ (NPTWNO) with simultaneously improved ionic diffusivity and electronic conductivity achieves good rate capability and cyclability. Furthermore, to obtain an insight into the promising fast-rechargeability of NPTWNO, several in-depth studies, including galvanostatic intermittent titration technique (GITT), density functional theory (DFT) computational analysis and electrochemical impedance spectroscopy (EIS) experiment were performed. We believe that the IL-templated nanoporous structure can effectively boost the Li^+ diffusion kinetics, and the doped W^{+6} with higher valence than Ti^{4+} can greatly enhance the electronic conductivity based on the effect of charge redistribution. Thereby, the assembled half cells and full cells indeed deliver good electrochemical performance.

Results and Discussion

Figure 1 presents the synthesis schematic diagram of NPTWNO material. Typically, in the proposed ionothermal synthesis-assisted doping strategy, titanium (IV) n-butoxide ($Ti(OBu)_4$), niobium (V) chloride ($NbCl_5$), tungsten (VI) chloride were mixed in IL [BMIm][NTf_2] and ethanol for a facile sol-gel process, followed by an IL recycling and air-calcination treatments. Noticeably, the IL concurrently acts as the nanoporous structure directing template and solvent, which is attributed to the favorable intermolecular interactions and promising solvent miscibility, respectively. Moreover, owing to the solvent miscibility, thermal stability and chemical stability of IL, the applied IL can be successfully removed and recycled from the gelled
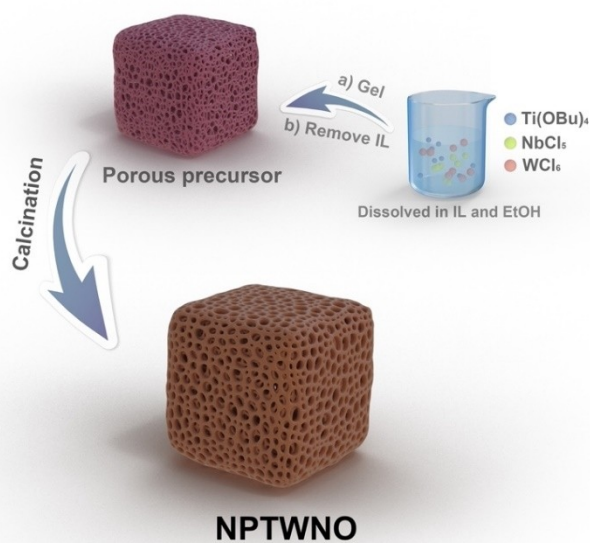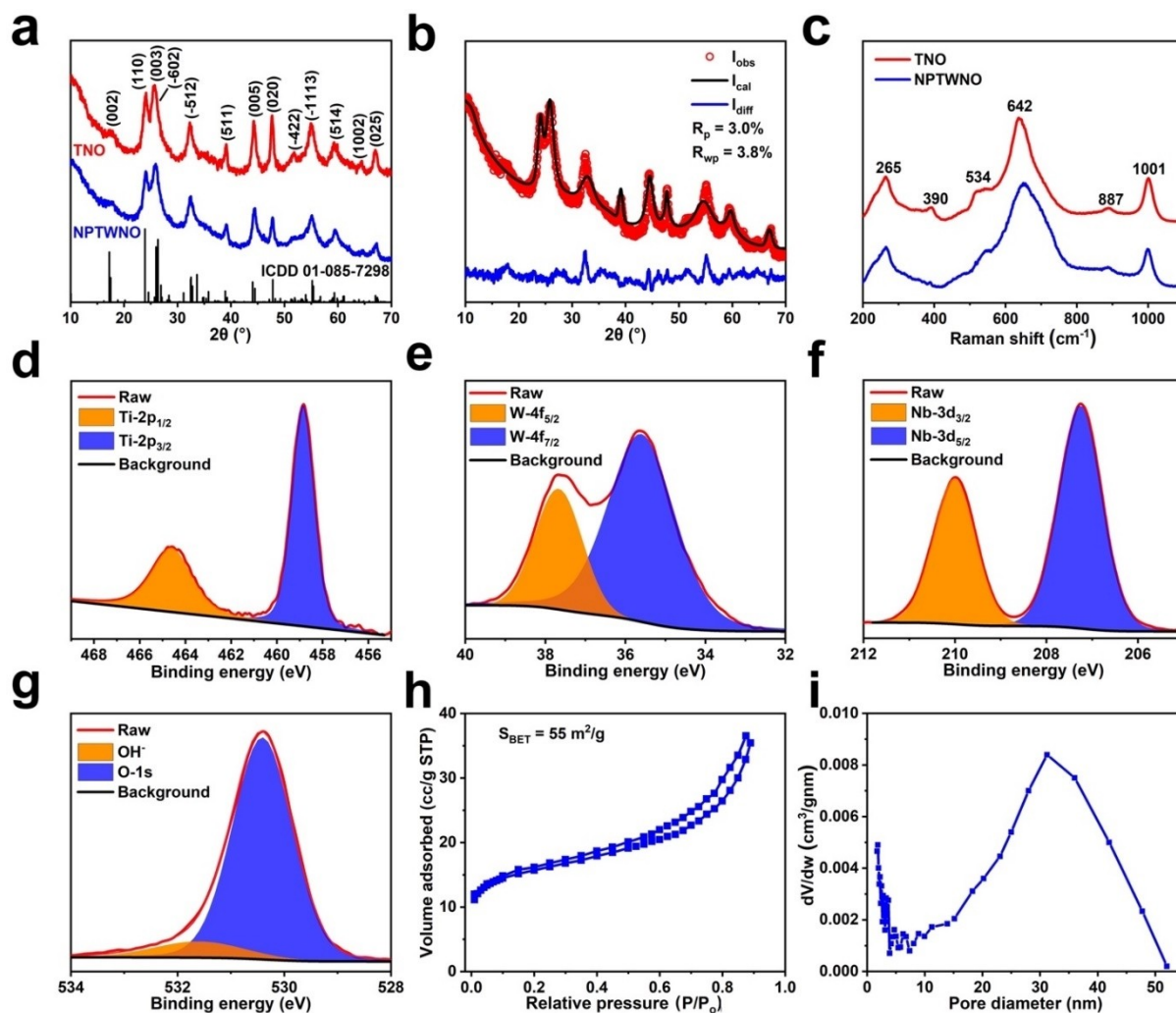
precursor based on a simple organic solvent wash, which leads to the formation of porosity and is eco-friendly. This is in sharp contrast with the traditional soft and/or hard templates that respectively causes considerable CO_2 emission due to the burning of co-block polymers and environmental and safety concerns of the usage of highly toxic etching agents, such as NaOH and HF.[8d]

As shown in Figures 2(a) and S1, the obtained X-ray diffraction (XRD) patterns of NPTWNO, NPTNO and TNO are highly similar, which conforms to the standard XRD pattern (ICDD 01-085-7298), belonging to the monoclinic family with prismatic shape and sharing the point group of C2/m. As the XRD Rietveld refinements shown in Figures 2(b), S2 and Table S1, the variations of lattice parameters and unit cell volume between TNO and NPTWNO can be attributed to the W^{6+} doping.[8a,b,9,10] To obtain a better understanding of the W^{6+}-doped material, Raman spectroscopy was employed to further analyze the structural information. Figure 2(c) shows the normalized Raman spectra of NPTWNO and TNO materials in the range between 200 and 1100 cm^{-1}. The similar widths of the peaks indicate that those two materials share similar crystallinity. The two characteristic peaks at 1001 and 887 cm^{-1} belong to the metal−oxygen stretching of edge/corner-shared NbO_6 octahedra, respectively.[11] The three peaks at 642, 534, and 390 cm^{-1} are attributed to the metal-oxygen stretching of TiO_6 octahedra.[12] Interestingly, the peak broadening at 642 cm^{-1} on the NPTWNO spectrum can be corresponded to the increased distribution of phonon energy states due to the W^{6+} dopant's disruption of long-range translational symmetry.[13] Moreover, the variations of peaks' intensities at around 534 and 390 cm^{-1} also indicate the presence of W^{6+} in the crystal lattice. In other words, a small amount of the W^{6+} successfully occupies the Ti^{4+} sites, thereby causing differences in the metal−oxygen stretching of TiO_6 octahedra based on the mass effect and variation of bond polarizability.[14] Lastly, the peaks around 265 cm^{-1} are ascribed to the symmetric and antisymmetric bending vibrations of O−Ti−O and O−Nb−O.[8c,11,12] Furthermore, to characterize the transition metal atomic ratio of NPTWNO, inductively coupled plasma-atomic emission spectroscopy (ICP-AES) was applied, which suggests the ratio of Ti, W and Nb is close to 0.95:0.05:2, respectively.

X-ray photoemission spectroscopy (XPS) was further applied to characterize the oxidation states of Ti, W, Nb, and O elements of NPTWNO. The broad XPS spectra of NPTWNO material are displayed in Figure S3(a), indicating the presence of Ti, W, Nb and O elements in the material. Figure 2(d–g) presents the high resolution XPS (HRXPS) of the four elements above. The two XPS peaks located at 464.6 eV and 458.8 eV in Figure 2(d) are ascribed to Ti-2$p_{1/2}$ and Ti-2$p_{3/2}$, and their binding energy difference of 5.8 eV reveals an oxidation state of Ti^{4+} in the material.[7b] As shown in Figure 2(e), the peaks at 37.7 and 35.6 eV correspond to W-4$f_{5/2}$ and W-4$f_{7/2}$, respectively, and the splitting of the spin orbit is about 2.1 eV, which uncovers W atom's valence state of $+6$ in the NPTWNO lattice.[15] The Nb-3$d_{3/2}$ and Nb-3$d_{5/2}$ peaks are detected at 210.0 and 207.3 eV, suggesting that the Nb in NPTWNO is pentava-

Figure 1. Schematic representation of the ionothermal synthesis strategy for with IL as the nanoporous structure directing template.

Figure 2. Typical characterizations of NPTWNO material. a) XRD patterns of TNO and NPTWNO. b) XRD Rietveld refinement of NPTWNO. c) Raman spectra of TNO and NPTWNO. d–g) HRXPS spectra of Ti, W, Nb and O for NPTWNO, respectively. h and i) Nitrogen adsorption-desorption isotherm profile and corresponding BJH plot of NPTWNO, respectively.

lent (Figure 2f).[3a,16] The peaks at 530.4 and 531.7 eV in Figure 2(g) can be assigned to O-1 s and trace-water OH−, respectively.[17] Notably, as shown in Figure S3(b–d), the HRXPS data of TNO is highly similar to the aforementioned HRXPS results of Ti-2p, Nb-3d and O-1 s of NPTWNO. Therefore, based on the aforementioned studies, it is confirmed that the W^{6+} species is successfully doped into the TNO crystal lattice by occupying the Ti^{4+} sites in TiO_6 octahedra, leading to the formation of $Ti_{0.95}W_{0.05}Nb_2O_7$ species.

To further investigate the IL-templated nanoporous architecture, several characterizations were performed. The nitrogen sorption isotherm profile of NPTWNO is presented in Figure 2(h), and the observed IUPAC H4 type isotherm reveals that the obtained NPTWNO has internal porosity with three-dimensional intercrystalline mesopores.[18] The calculated Brunauer-Emmett-Teller (BET) specific surface area is 55 m^2 $g^{−1}$. This is much higher than that of the TNO. The corresponding Barrett-Joyner-Halenda (BJH) pore size distribution plot is shown in Figure 2(i), illustrating the presence of a main pore diameter of 31.2 nm. Notably, these aforementioned features of NPTWNO are in sharp contrast with the TNO which exhibits bulk feature (Figure S4a and b), demonstrating the effectiveness of IL. The obtained mesopores can be attributed to the occupied space of the IL template based on the hydrogen bonding between IL's anions and precursors and the neighboring imidazolium rings' π–π stack interactions of ILs.[7a,b] The mesoporous structure can facilitate the contact between electrode and electrolytes, ensuring unhindered Li^+ diffusion pathways.[2b,7b,19]

To further reveal the crystallite sizes, morphologies and microstructures of the synthesized materials, scanning electron microscopy (SEM) and transmission electron microscopy (TEM) were employed. The SEM image displayed in Figure 3(a) shows the three-dimensionally porous structure of the obtained NPTWNO. Additionally, NPTWNO material presents a typical secondary structure, containing micrometer-scale particles agglomerated by NPTWNO nanocrystallites that have an average size of 20 nm. NPTNO material (Figure S3) shares similar structural features. Moreover, the SEM energy dispersive
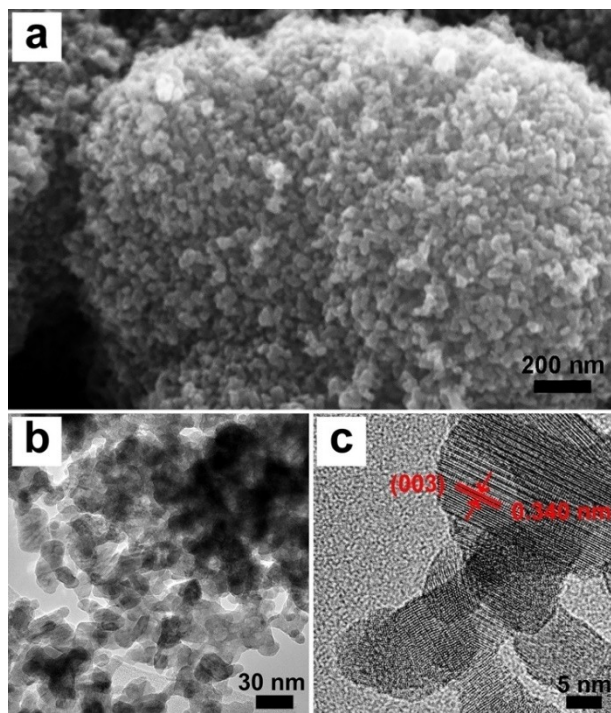
Figure 3. a) SEM, b) TEM and c) HRTEM images of NPTWNO, respectively.

X-ray spectroscopy (EDX) analyses reveal the existence and even distribution of Ti, W, Nb and O elements in NPTWNO material (Figure S6), being consistent with the XPS results above. Figure 3(b) reveals that the size distribution of NPTWNO nanocrystallites is relatively homogeneous. In sharp contrast, the SEM and TEM images of the prepared TNO material only present bulk feature (Figure S7). As shown in Figure 3(c), the observed lattice fringes on the NPTWNO nanocrystallite indicate the appearance of a well-defined crystal structure. Notably, as shown in Figure S8(a and b), the NPTNO material exhibits comparable microstructure in the TEM and HRTEM images, respectively, implying the W^{6+}-dopant in NPTWNO material does not have a huge impact on the nanocrystallites and their formed framework. Particularly, the measured lattice fringe space is about 0.340 nm, which is assigned to the crystallographic planar of (003), sharing coherence with the aforementioned XRD results. Noticeably, the selected area electron diffraction (SAED) patterns of NPTWNO (Figure S9a) and TNO (Figure S9b) are highly comparable due to the belonged identical crystal structure system, which further confirms the XRD results above.

To investigate the electrochemical performance of the synthesized NPTWNO material, LIB half cells were assembled and tested. As shown in Figure 4(a), cyclic voltammetry (CV) was conducted to study the electrochemical properties of NPTWNO electrode. The broad peaks at 1.0–1.4 V are ascribed to the Nb^{4+}/Nb^{3+} redox couple.[20] The large redox at 1.73 and 1.57 V are attributed to the Nb^{5+}/Nb^{4+} redox couple.[21] The two small sharp peaks at 2.00 and 1.73 V are assigned to the reaction of Ti^{4+}/Ti^{3+}.[22] These observed peaks also appear on
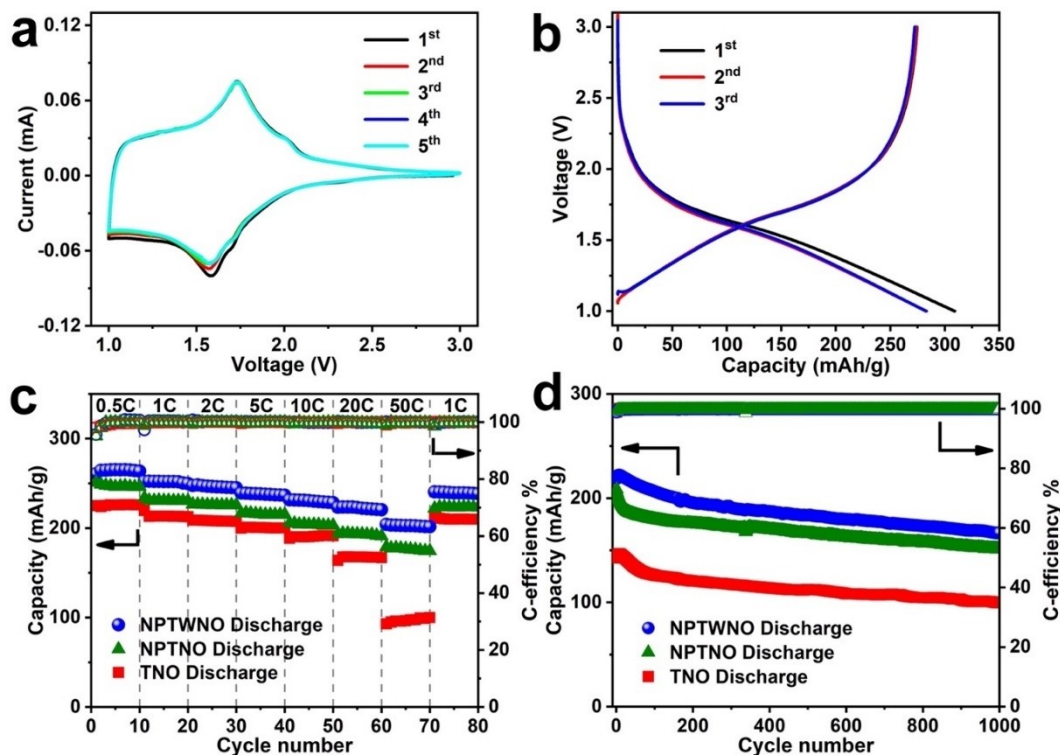

Figure 4. Electrochemical characterizations of assembled half cells. a) CV profiles at a scan rate of 0.05 mV s^{-1}. b) The initial galvanostatic discharge/charge curves at 0.1 C. c) Rate performance of NPTWNO, NPTNO and TNO at various rates: discharge current rate fixed at 1 C (except the 0.5 C discharge/charge profile). d) Cyclic performance of NPTWNO, NPTNO and TNO at a constant current rate of 5 C after aging at 0.1 C for 3 cycles.

Batteries & Supercaps

Research Article
doi.org/10.1002/batt.202300101

Chemistry
Europe

European Chemical
Societies Publishing

the CV profile of the TNO material (Figure S10), indicating the prepared materials share the same electrochemical redox reactions. Furthermore, the overlapped CV profiles after the first cycle suggest that the obtained NPTWNO has excellent electrochemical and cycling stability.[18a] Notably, the slight reduction peak shift after the first cycle corresponds to the migration of the Fermi level and major distortion of the metal-oxygen octahedra during the Li$^+$ insertion process.[3b,23]

Figure 4(b) presents the galvanostatic discharge/charge curves of the first three cycles in the range of 1.0–3.0 V at 0.1 C (38.7 mA g^{-1}). A discharge plateau appears around 1.65 V, correlating to a solid-solution phase transition process (the transformation from solid-solution phase (SS1) to two-phase coexistence (SS1 and SS2) occurs within voltage range from 1.70 to 1.65 V, and the transition from two-phase coexistence (SS1 and SS2) to solid-solution phase (SS2) happens within voltage range from 1.65 to 1.60 V).[2b,3b,7b,24] The initial discharge (Li$^+$ insertion) and charge (Li$^+$ extraction) capacities are 309 and 275 mA h g^{-1}, corresponding to a coulombic efficiency of 89.0%. Moreover, unlike TNO only delivering a reversible capacity of 245 mA h g^{-1} (Figure S11), NPTWNO achieves a reversible capacity of 283 mA h g^{-1}, which is close to that of graphite and is significantly higher than that of LTO.[2b]

Figure 4(c) shows the rate performance of the prepared TNO, NPTNO and NPTWNO electrodes. The obtained average discharge capacities of TNO at 20 and 50 C are 167 and 97 mA h g^{-1}, correspondingly. As expected, with the assistance of nanoporous structure, NPTNO (Figure S12a and b) presents much better performance at high rates. At 20 and 50 C, high average discharge capacities of 193 and 176 mA h g^{-1} are observed, respectively. More impressively, with the assistance of the doped W^{6+} cations, NPTWNO indeed displays improved rate capability, which respectively delivers average discharge capacities of 222 and 203 mA h g^{-1} at 20 and 50 C. Notably, the achieved rate capability is competitive (Table S2). Thereby, the enhanced rate performance of NPTWNO is attributed to the enhanced Li$^+$ diffusivity and improved electronic conductivity.

To investigate the cyclability of the obtained materials, long-term cycling tests at 5 C were performed (Figure 4d). For TNO, the obtained capacities of the first and 1000th cycles are 144 and 99 mA h g^{-1}, respectively, reflecting a capacity retention of 69%. In sharp contrast, with NP structure, NPTNO and NPTWNO materials exhibit enhanced long-term cyclability at high rate. Specifically, NPTNO respectively delivers 208 and 151 mA h g^{-1} in the initial and final cycles. This indicates the capacity retention is about 72%. Moreover, high capacities of 218 and 167 mA h g^{-1} in the first and 1000th cycles with a capacity retention of 77% are achieved in the NPTWNO-based cell, correspondingly. Such good cyclability of NPTWNO is not only due to the excellent structural integrity and stability of its nanoporous architecture but also rooted in the facilitated electrochemical kinetics based on the W^{6+} doping.[7b,25]

To illustrate the boosted Li$^+$ diffusion kinetics of NPTWNO based on the nanoporous structure, galvanostatic intermittent titration technique (GITT) was employed for the quasi-in-situ probing of Li$^+$ diffusion kinetics during the lithiation process. Figure 5(a) and its inset display two typical discharge steps of

the NPTWNO-based half cell. The rapid voltage drop is attributed to the iR drop, and the following slow potential decrease is ascribed to the galvanostatic discharge current pulse. While during the relaxation, the quick potential increase is assigned to the iR followed by a slow increase until a stable status. Thereby, it is confirmed that the 1-h relaxation with 200-s pulse is long enough to allow the electrode to reach the equilibrium statues. Accordingly, the Li$^+$ diffusion coefficient is via the following equation,

$$D = \frac{4}{\pi\tau}\left(\frac{n_m V_m}{S}\right)^2\left(\frac{\Delta E_s}{\Delta E_t}\right)^2 \tag{1}$$

where D, τ, n_m, V_m, S, ΔE_s and ΔE_t are the Li$^+$ diffusion coefficient, the duration of the current pulse (s), the number of moles (mol), the molar volume of the active material (cm^3/mol), the electrode/electrolyte contact area (cm^2), the equilibrium voltage change induced by current pulse and the voltage change during the constant current pulse (neglecting the iR drop), respectively.[24,26] As shown in Figure 5(b), NPTWNO presents the fastest Li$^+$ diffusion kinetics among the three prepared electrodes. Notably, the Li$^+$ diffusivity of NPTWNO and NPTNO is considerably higher than that of the bulk TNO, which further confirms the advantage of the nanoporous feature. During the lithiation (discharge), a huge drop of D_{Li^+} value is observed at around 1.65 V. This is in line with some pioneering work and the CV analysis above, which is rooted in the typical solid-solution phase transition of metal oxides with Wadsley Roth phases.[2b,7b,8d,15d,24]
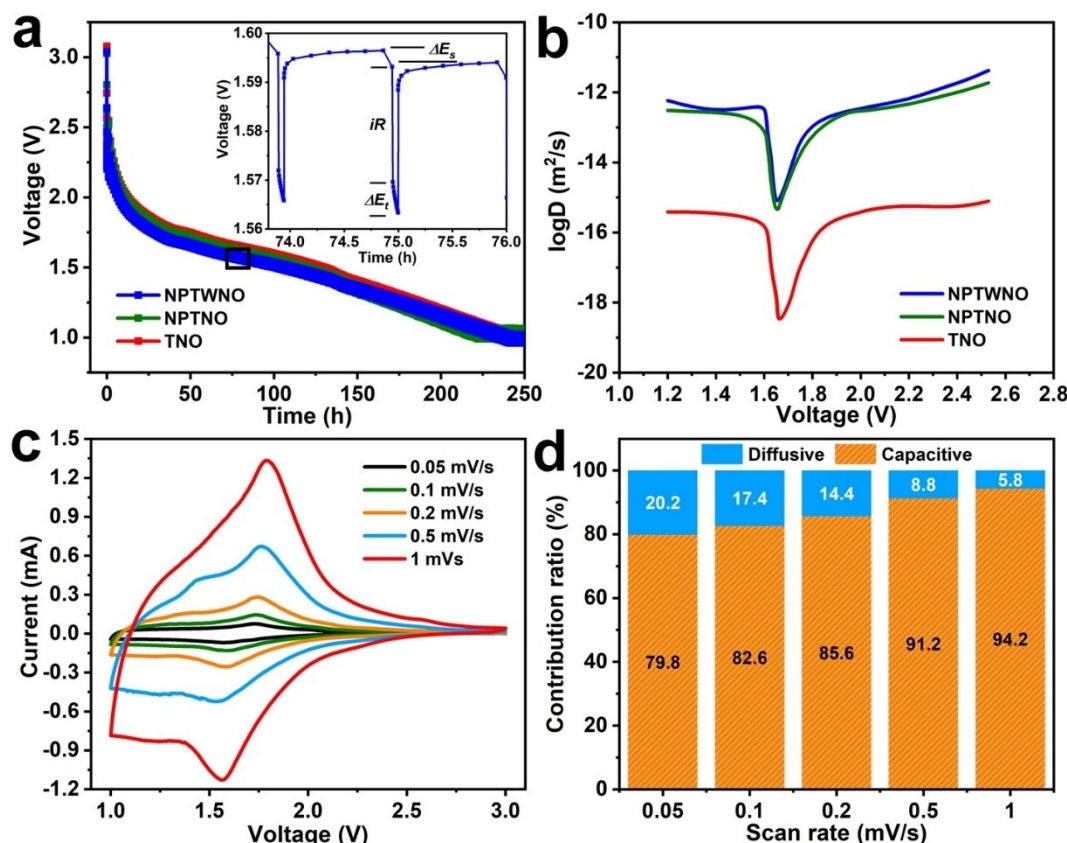
Furthermore, to characterize the surface-induced capacitive contribution, CV tests at various scan rates were performed (Figures 5c and S13a). Typically, the current of the cathodic and anodic peaks gradually increases along with the scan rates. Furthermore, the following Equation (2) and its derived Equation (3) were applied to quantitatively analyze the contribution of the diffusive and capacitive behaviors,

$$i(V) = k_1 v + k_2 v^{1/2} \tag{2}$$

$$i(V)/v^{1/2} = k_1 v^{1/2} + k_2 \tag{3}$$

where, k_1 and k_2 are adjustable parameters, and $i(V)$, $k_1 v$ and $k_2 v^{1/2}$ are the total current at a fixed potential, the capacitive contribution and the diffusive contribution, respectively.[3b,27] Accordingly, as shown in Figures 5(d) and S13(b), along with the increase of the scan rates from 0.05 to 1 mV s^{-1}, the proportion of surface capacitive contribution for NPTWNO and TNO increases along with the increase of scan rate. Notably, such increase trend of capacitive contribution is in line with some pioneering work.[28]

To further obtain an atomic insight into the improved electronic conductivity of the obtained NPTWNO material due to bandgap narrowing, a density functional theory (DFT) computational study was carried out on Ti$_{18}$Nb$_{36}$O$_{126}$ and Ti$_{17}$W$_1$Nb$_{36}$O$_{126}$ supercells based on five potential Ti^{4+} occupational sites in TNO lattice (Figure 6a), denoted as M1, M2, M3, M4 and M5 by following the notation of Prof. Clare P. Grey's

Batteries & Supercaps

Research Article
doi.org/10.1002/batt.202300101

Chemistry Europe
European Chemical
Societies Publishing

Figure 5. a and b) GITT profiles of the prepared electrodes and their corresponding Li^+ diffusivity, respectively. c) CV profile of NPTWNO at various scan rates. d) Contribution of the capacitive and diffusive behaviors for NPTWNO at various scan rates.
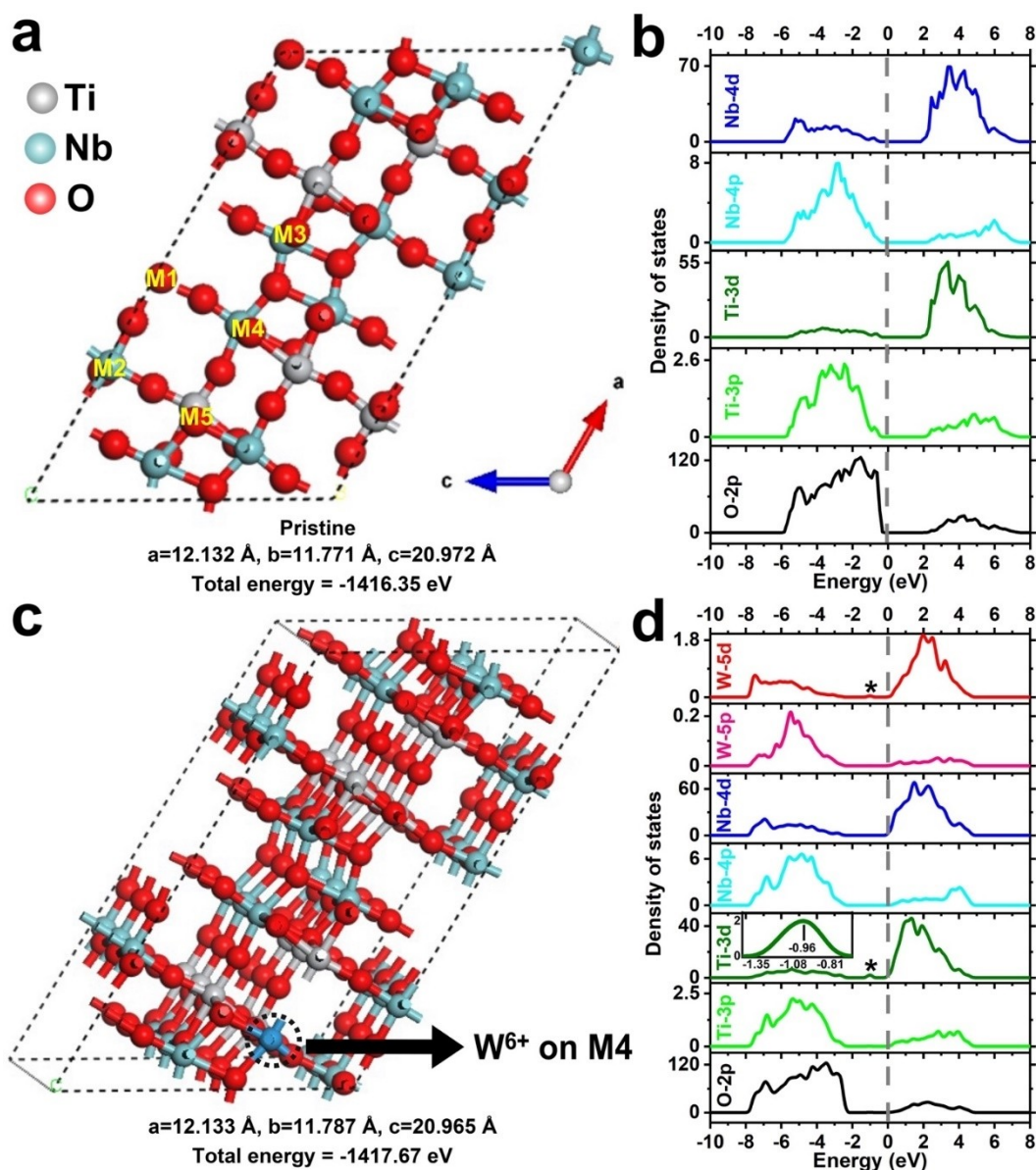
pioneering work.[29] Typically, as the projected density of states (PDOS) displayed in Figure 6(b), in the case of parent $Ti_{18}Nb_{36}O_{126}$ with Ti^{4+} occupying on the $M4$ and $M5$ sites, the computed conduction-valence bandgap of TNO is about 2.6 eV, which thereby causes the low electronic conductivity and poor high rate-capability of TNO. After doping W^{6+} into TNO lattice on one Ti^{4+} site and forming the WO_6 octahedra observed in Raman spectroscopy study, as shown in Figure 6(c and d), W^{6+} on the $M4$ site is more thermodynamically preferable with the lowest total energy, which is 0.85 eV lower than that of W^{6+} residing on the $M5$ site (Figure S14), thereby leading to an obvious reconstruction of the conduction and valence bands nearing the Fermi-level. Noticeably, a continuous conduction band indeed crosses the Fermi-level, suggesting that the W^{6+}-doped TNO would more likely be in metallic state and exhibits high electronic conductivity. Additionally, the small bands overlapping of Ti-3d and W-5d orbitals are observed at -0.96 eV, indicating the successful hybridization of those two orbitals. It is interesting to note that such phenomenon does not appear in other doping cases and is in sharp contrast with the large bandgap observed in the pristine TNO, potentially revealing the reason why such atomic arrangement is the most possible and favorable doping case. Moreover, comparing to the case that Ti^{4+} occupies on the M5 and M2 sites (Figure S15), as shown in Figure S16 and S17, respectively, even on unfavorable doping sites, W^{6+} doping can also induce the

reconstruction and shifting of the bands that cross the Fermi-level, forming into metallic state.[8d] Thereby, those aforementioned results elucidate that the electronic conductivity of NPTWNO material is dramatically enhanced, due to the narrowed conductive-valence bandgap induced by the formation of the dopant's impurity band together with appearance of metallic state.

Additionally, the W^{6+} doping induced electrical conductivity enhancement is also confirmed by an electrochemical method. As shown in Figure S18, the EIS data of NPTWNO indeed presents a smaller Ohmic impedance than those of the TNO and NPTNO electrodes in the high-frequency region, suggesting that the electrical conductivity is indeed improved due to the W^{6+} doping.[8a,30] In the mid-high-frequency area, the charge transfer impedances of NPTNO and NPTWNO are significantly lower than that of TNO, especially NPTWNO. This is directly ascribed to the enlarged electrode-electrolyte contact area that can facilitate the mass transfer in the cells.[31] In the low-frequency region, NPTWNO and NPTNO also present faster Warburg diffusion kinetics than the TNO with bulk feature does, reflecting the aforementioned excellent rate performance study. The ZFit in EC-Lab software reveals that the prepared half cell configurations correspond to the typical Randles circuit.

To further characterize the practicality of the synthesized NPTWNO material and the proposed preparational strategy,

Batteries & Supercaps

Research Article
doi.org/10.1002/batt.202300101

Chemistry Europe
European Chemical
Societies Publishing

Figure 6. DFT computational study. a) Pristine TNO lattice structure with the symmetrically distinct transition metal (*M*) sites, according to the nomenclature of Perfler et al.[12] b) PDOS of the pristine TNO with Ti^{4+} on the *M*5 and *M*4 sites. c and d) Doped TNO lattice structure with Ti^{4+} on the *M*5 and *M*4 sites and W^{6+} on *M*4 site and its corresponding PDOS, respectively.

high-voltage spinel $LiNi_{0.5}Mn_{1.5}O_4$ (LNMO) cathode was coupled with NPTWNO anode for the full cell study. As shown in Figure 7(a), the observed voltage plateau is at about 3.0 V, implying the high energy density of the full cells. A reversible discharge specific capacity of 239.5 mAh g^{-1} is achieved at a current density of 1 C. These suggests that the assembled coin cell delivers a good energy density of 203.3 Wh kg^{-1}, which is higher than some reported Wadsley-Roth phased materials.[7c,32] As shown in Figure 7(b), at current densities of 0.5, 1, 2, 5, 10 and 20 C, the average discharge specific capacities of LNMO-NPTWNO cell are 258.2, 247.0, 192.6, 148.0, 103.9 and 48.2 mAh g^{-1}, respectively. Interestingly, a high average discharge specific capacity of 243.2 mAh g^{-1} is indeed achieved at the recovery 1 C, which directly reflects the excellent electro-

chemical reversibility of the full cell. Figure 7(c) displays the long-term cyclability of the LNMO-NPTWNO cell over 800 cycles at a high constant current density of 10 C. The full cell exhibits good specific capacities of 108.3 and 87.4 mAh g^{-1} in the initial and final cycles, respectively. Such result indicates that the 800-cycle capacity retention rate is 80.1 %. Moreover, as presented in Figures 7d and S20, the assembled high-loading pouch cell can be stably cycled over 200 cycles at 1 C. Thereby, the aforementioned full cell studies successfully demonstrate the practicality of the synthesized NPTWNO material and the proposed preparational strategy.

In light of the pre-mentioned electrochemical results and mechanism analysis, the origins of the excellent rate capability of the obtained NPTWNO material can be attributed to two
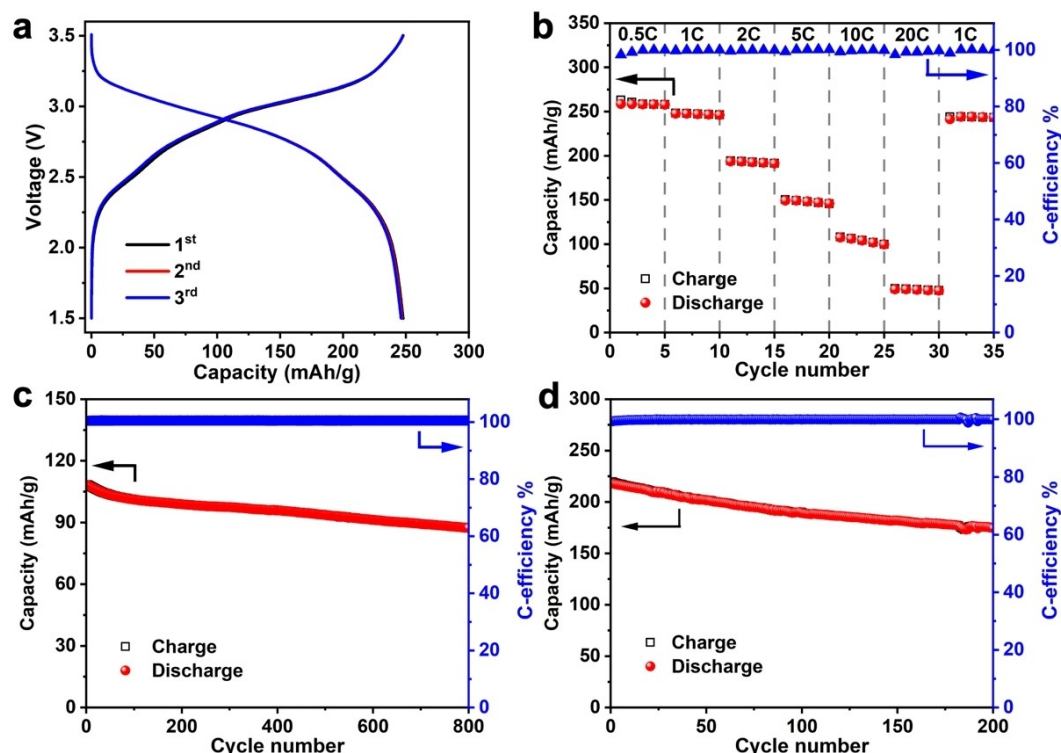
Figure 7. NPTWNO-LNMO full cell studies. a) Galvanostatic charge/discharge curves at 1 C. b) Rate performance test at various current rates. c) Cyclic performance at a constant charge/discharge current rate of 10 C over 800 cycles. d) Pouch cell cycling profile at 1 C.

major aspects: the unhindered Li^+ diffusion kinetics induced by the nanoporous structure and the improved electronic conductivity based on the charge redistribution effect of doping W^{6+}. Firstly, the mesoporous structure composed of W^{6+}-doped TNO nanocrystals from templating IL not only significantly reduces the Li^+ diffusion distance but also enlarges the electrode-electrolyte contact, ensuring a straightforward Li^+ insertion-extraction kinetics. Secondly, the doping W^{6+} into the TNO crystal lattice generates an impurity band between the conduction and valence bands, and consequently the electronic conductivity is dramatically boosted due to the bandgap narrowing induced by charge redistribution. Moreover, the TNO lattice structural and electrochemical stabilities are well-maintained after the W^{6+} doping, ensuring the fast-charging potential. Last but not least, the nanoporous structure of NPTWNO can benefit its cyclability based on the alleviation of the repetitive mechanical stress and volume fluctuation from the Li^+ insertion-extraction processes.

Conclusions

In summary, this study indicates the potential of ionothermal synthesis in energy storage materials, which enables the concurrent improvements of the electronic and ionic conductivities. Accordingly, the novel W^{6+}-doped nanoporous $TiNb_2O_7$ material achieves a good rate performance of 222 and 203 mAh g^{-1} at 20 and 50 C, respectively. Moreover, besides high rate capability, the synthesized NPTWNO also delivers an excellent high-rate long-term cyclability of 77% capacity retention over 1000 cycles at 5 C. Furthermore, the coin cell and pouch cell-based LIB full cell tests indeed achieve good electrochemical performance, confirming the practicality of the proposed material and synthetic strategy. Such promising results are mainly attributed to the improved electronic conductivity rooted in the charge redistribution effect of doping W^{6+} and the enhanced Li^+ diffusion kinetics induced by the IL-templated nanoporous structure, which are well-demonstrated in the GITT, DFT and EIS studies. Therefore, we believe that this ionothermal synthesis-assisted doping strategy paves an avenue for the development of LIB fast-rechargeable anode materials.

Experimental Section

Synthesis of nanoporous $Ti_{0.95}W_{0.05}Nb_2O_7$ (NPTWNO) material: Starting reagents 1.617 g of $Ti(OC_4H_9)_4$, 0.0992 g of WCl_6 and 2.702 g of $NbCl_5$ were dissolved in 12.0 g of [BMIm][NTf$_2$] IL and 10 mL of ethanol and vigorously stirred for 12 h. Subsequently, the solution was gelled in a Petri dish at 50 °C followed by a 2 h aging at 200 °C. Next, the templating [Bmim][NTf$_2$] was extracted and recycled from sample by ethanol wash and rotary evaporation. Lastly, the washed sample was calcined at 700 °C in air for 3 h (ramp rate 2 °C min^{-1}) to obtain the NPTWNO material.

Synthesis of nanoporous $TiNb_2O_7$ (NPTNO) material: The preparation is identical to the synthesis of NPTWNO, except for dissolving 1.702 g of $Ti(OC_4H_9)_4$ with 2.702 g of $NbCl_5$ in 9.0 g of IL and 10 mL of ethanol.

Batteries & Supercaps

Research Article
doi.org/10.1002/batt.202300101

Chemistry
Europe

European Chemical
Societies Publishing

Synthesis of bulk TiNb$_2$O$_7$ (TNO) material: The preparation is identical to the synthesis of NPTNO without using IL.

Typical characterizations: The crystal structures of the obtained materials were characterized by powder X-ray diffraction (XRD, Panalytical Empyrean diffractometer at conditions of 45 kV and 40 mA). The recorded XRD patterns were analyzed by High Score Plus. Raman spectra were acquired from a WITec GmbH Alpha 300 confocal Raman microscope with a solid-state 532 nm excitation laser. X-ray photoelectron spectroscopy (XPS) analyses were performed on a ULVAC PHI XPS apparatus equipped with Al K_α radiation (1486.6 eV) to examine valance states of elements of the prepared materials. The energy calibration and deconvolution of XPS peaks were carried out by CasaXPS (Casa Software Ltd). Nitrogen isothermal adsorption-desorption data was measured on a TriStar 3000 volumetric adsorption analyzer from Micromeritics Instrument Corp. Scanning electron microscope (SEM) imaging was conducted on a Carl Zeiss Auriga 40 SEM microscope. Inductively coupled plasma-atomic emission spectroscopy (ICP-AES) data was measured on an Optima 2100 DV spectrometer (PerkinElmer Corporation). SEM energy dispersive X-ray spectroscopy (EDX) studies were performed on a Carl Zeiss EVO MA15. Transmission electron microscope (TEM) images were collected on a Carl Zeiss Libra 200 MC TEM microscope. An Agilent 700 series inductively coupled plasma-atomic emission spectroscopy (ICP-AES) from Agilent Technologies, Inc, was applied to analyze the ratio of the elements.

Density functional theory (DFT) computational studies of projected density of states (PDOS): All the computational studies were performed with the generalized gradient approximation (GGA) of the Perdew–Burke–Ernzerhof (PBE) exchange-correlation functional as implement in the Ab-Initio Simulation Package (VASP) code. The projected augmented wave (PAW) pseudopotentials were utilized to describe the core and valence electrons using a plane-wave kinetic energy cut-off of 500 eV. DFT+U computation was applied with the Coulomb (U) and exchange (J) parameters are treated separately. The parameter J with value of 1.0 eV was used for all computations in this work. Two sets of parameter U values were applied in this work: a U correction of 5.0 eV was applied to Ti element, and a U correction of 5.2 eV was applied to both Ti and Nb, based on a previous study from Prof. Clare P. Grey's group.[29] The structures were allowed to relax with the convergence criteria for the energy of 1×10^{-6} eV, and the force convergence criteria was set as 0.02 eV Å^{-1}.

Electrochemical property studies: The sample electrodes for coin cells and high-loading pouch cells were prepared with the obtained anode materials, Super C 65TM carbon black and polyvinylidene fluoride (PVDF) at mass ratios of 80:10:10 and 92:3:5, respectively. The n-methylpyrrolidone-based slurry was then casted onto Cu foils and dried under an infrared lamp to remove the solvent, followed by a 120 °C vacuum oven drying for 12 h. The weight loading of the active material on the fabricated electrodes for coin cells and pouch cells were around 1.5 and 10.2 mg cm^{-2}, respectively. The CR2032-type coin cells were assembled by pairing the as-prepared electrodes to lithium counter electrode inside an argon-filled glove box with H$_2$O and O$_2$ contents less than 1 ppm. Celgard 2500 was used as the separator. Gen2 electrolyte was used (1.2 M of LiPF$_6$ in ethylene carbonate (EC)/ ethyl methyl carbonate (EMC) with a weight ratio of 3/7, from Tomiyama Pure Chemical Industries, LTD). The LIB half cells galvanostatic discharge/charge tests were carried out at various C-rates in the voltage range of 1.0–3.0 V on a Maccor Series 4000 tester. Cyclic Voltammetry (CV) tests with potential range of 1.0–3.0 V were carried out on a BioLogic MPG2 system. Electrochemical impedance spectroscopy (EIS) data was collected on a BioLogic MPG2 system and then analyzed by the ZFit tool in EC-Lab V11.43

software. The high-voltage spinel LiNi$_{0.5}$Mn$_{1.5}$O$_4$ (LNMO) cathode (the mass ratio of LNMO, Super C 65TM carbon black and PVDF is 90:5:5, respectively)-coupled full cells were assembled at N:P ratio of around 1:1.1. Celgard 2500 and Gen2 electrolyte were used as the separator and electrolyte. The coin cells were assembled in an argon-filled glove box with H$_2$O and O$_2$ contents less than 1 ppm. The assembly of high-loading (4.5 cm×5.5 cm) single-layer pouch cell was performed in the dry room with control environment (relative humidity < 0.1 %) at Oak Ridge National Laboratory Battery Manufacturing R&D Facility. The LIB full cells galvanostatic charge/discharge tests were carried out at various C-rates in the voltage range of 1.5–3.5 V on a Maccor Series 4000 tester.

Conflict of Interests

The authors declare no conflict of interest.

Data Availability Statement

The data that support the findings of this study are available on reasonable request from the corresponding author. The data are not publicly available due to privacy or ethical restrictions.

[1] a) M. M. Thackeray, C. Wolverton, E. D. Isaacs, *Energy Environ. Sci.* **2012**, *5*, 7854–7863; b) H. Liu, R. Tao, C. Guo, W. Zhang, X. Liu, P. Guo, T. Zhang, J. Liang, *Chem. Eng. J.* **2022**, *429*, 132239; c) J. Liang, R. Tao, J. Tu, C. Guo, K. Du, R. Guo, W. Zhang, X. Liu, P. Guo, D. Wang, S. Dai, X.-G. Sun, *J. Mater. Chem. A* **2022**, *10*, 12563–12574; d) S. Chen, R. Tao, C. Guo, W. Zhang, X. Liu, G. Yang, P. Guo, G. Sun, J. Liang, S.-Y. Lu, *Energy Storage Mater.* **2021**, *41*, 758–790.

Batteries & Supercaps

Research Article
doi.org/10.1002/batt.202300101

Chemistry
Europe
European Chemical
Societies Publishing

[2] a) H. Yu, H. Lan, L. Yan, S. Qian, X. Cheng, H. Zhu, N. Long, M. Shui, J. Shu, *Nano Energy* **2017**, *38*, 109–117; b) B. Guo, X. Yu, X.-G. Sun, M. Chi, Z.-A. Qiao, J. Liu, Y.-S. Hu, X.-Q. Yang, J. B. Goodenough, S. Dai, *Energy Environ. Sci.* **2014**, *7*, 2220–2226; c) G. Yang, R. Tao, C. J. Jafta, C. Shen, S. Zhao, L. He, I. Belharouak, J. Nanda, *J. Phys. Chem. C* **2021**, *125*, 13146–13157; d) G. Yang, S. Frisco, R. Tao, N. Philip, T. H. Bennett, C. Stetson, J.-G. Zhang, S.-D. Han, G. Teeter, S. P. Harvey, Y. Zhang, G. M. Veith, J. Nanda, *ACS Energy Lett.* **2021**, *6*, 1684–1693; e) H. Liu, Z. Zhu, Q. Yan, S. Yu, X. He, Y. Chen, R. Zhang, L. Ma, T. Liu, M. Li, R. Lin, Y. Chen, Y. Li, X. Xing, Y. Choi, L. Gao, H. S.-y. Cho, K. An, J. Feng, R. Kostecki, K. Amine, T. Wu, J. Lu, H. L. Xin, S. P. Ong, P. Liu, *Nature* **2020**, *585*, 63–67.

[3] a) X. Wang, G. Shen, *Nano Energy* **2015**, *15*, 104–115; b) S. Lou, X. Cheng, Y. Zhao, A. Lushington, J. Gao, Q. Li, P. Zuo, B. Wang, Y. Gao, Y. Ma, C. Du, G. Yin, X. Sun, *Nano Energy* **2017**, *34*, 15–25; c) G. Zhang, H. Deng, R. Tao, B. Xiao, T. Hou, S. Yue, N. Shida, Q. Cheng, W. Zhang, J. Liang, *Mater. Lett.* **2020**, *262*, 127194.

[4] a) X. Wen, C. Ma, C. Du, J. Liu, X. Zhang, D. Qu, Z. Tang, *Electrochim. Acta* **2015**, *186*, 58–63; b) J.-T. Han, Y.-H. Huang, J. B. Goodenough, *Chem. Mater.* **2011**, *23*, 2027–2029; c) H. Li, L. Shen, G. Pang, S. Fang, H. Luo, K. Yang, X. Zhang, *Nanoscale* **2015**, *7*, 619–624; d) K. J. Griffith, Y. Harada, S. Egusa, R. M. Ribas, R. S. Monteiro, R. B. Von Dreele, A. K. Cheetham, R. J. Cava, C. P. Grey, J. B. Goodenough, *Chem. Mater.* **2021**, *33*, 4–18.

[5] A. Vu, Y. Qian, A. Stein, *Adv. Energy Mater.* **2012**, *2*, 1056–1085.

[6] a) X. Zhu, P. C. Hillesheim, S. M. Mahurin, C. Wang, C. Tian, S. Brown, H. Luo, G. M. Veith, K. S. Han, E. W. Hagaman, H. Liu, S. Dai, *ChemSusChem* **2012**, *5*, 1912–1917; b) J. S. Lee, X. Wang, H. Luo, G. A. Baker, S. Dai, *J. Am. Chem. Soc.* **2009**, *131*, 4596–4597; c) S. Zhou, Z. Ma, G. A. Baker, A. J. Rondinone, Q. Zhu, H. Luo, Z. Wu, S. Dai, *Langmuir* **2009**, *25*, 7229–7233; d) X. Cui, Q. Yang, Y. Xiong, Z. Bao, H. Xing, S. Dai, *Chem. Commun.* **2017**, *53*, 4915–4918; e) P. Zhang, H. Lu, Y. Zhou, L. Zhang, Z. Wu, S. Yang, H. Shi, Q. Zhu, Y. Chen, S. Dai, *Nat. Commun.* **2015**, *6*, 8446; f) Z. Ma, J. Yu, S. Dai, *Adv. Mater.* **2010**, *22*, 261–285; g) X. Wang, S. Dai, *Angew. Chem. Int. Ed.* **2010**, *49*, 6664–6668.

[7] a) Y. Zhou, J. H. Schattka, M. Antonietti, *Nano Lett.* **2004**, *4*, 477–481; b) R. Tao, G. Yang, E. C. Self, J. Liang, J. R. Dunlap, S. Men, C.-L. Do-Thanh, J. Liu, Y. Zhang, S. Zhao, H. Lyu, A. P. Sokolov, J. Nanda, X.-G. Sun, S. Dai, *Small* **2020**, *16*, 2001884; c) H. Lyu, J. Li, T. Wang, B. P. Thapaliya, S. Men, C. J. Jafta, R. Tao, X.-G. Sun, S. Dai, *ACS Appl. Energ. Mater.* **2020**, *3*, 5657–5665.

[8] a) H. Song, Y.-T. Kim, *Chem. Commun.* **2015**, *51*, 9849–9852; b) H. Song, S.-W. Yun, H.-H. Chun, M.-G. Kim, K. Y. Chung, H. S. Kim, B.-W. Cho, Y.-T. Kim, *Energy Environ. Sci.* **2012**, *5*, 9903–9913; c) J.-Y. Lin, C.-C. Hsu, H.-P. Ho, S.-h. Wu, *Electrochim. Acta* **2013**, *87*, 126–132; d) R. Tao, T. Zhang, S. Tan, C. J. Jafta, C. Li, J. Liang, X.-G. Sun, T. Wang, J. Fan, Z. Lu, C. A. Bridges, X. Suo, C.-L. Do-Thanh, S. Dai, *Adv. Energy Mater.* **2022**, *12*, 2200519; e) C. Yang, D. Ma, J. Yang, M. Manawan, T. Zhao, Y. Feng, J. Li, Z. Liu, Y.-W. Zhang, R. B. Von Dreele, B. H. Toby, C. P. d. L. Albarrán, J. H. Pan, *Adv. Funct. Mater.* n/a, 2212854; f) Y.-S. Hsiao, L.-Y. Chang, C.-W. Hu, C.-Z. Lu, N.-J. Wu, Y.-L. Chen, T.-H. Hsieh, J.-H. Huang, S.-C. Hsu, H.-C. Weng, C.-P. Chen, *Appl. Surf. Sci.* **2023**, *614*, 156155.

[9] C. Lin, S. Yu, S. Wu, S. Lin, Z.-Z. Zhu, J. Li, L. Lu, *J. Mater. Chem. A* **2015**, *3*, 8627–8635.

[10] a) C. Yang, C. Lin, S. Lin, Y. Chen, J. Li, *J. Power Sources* **2016**, *328*, 336–344; b) J. Gao, X. Cheng, S. Lou, Y. Ma, P. Zuo, C. Du, Y. Gao, G. Yin, *J. Alloys Compd.* **2017**, *728*, 534–540.

[11] N. G. Eror, U. Balachandran, *J. Solid State Chem.* **1982**, *45*, 276–279.

[12] L. Perfler, V. Kahlenberg, C. Wikete, D. Schmidmair, M. Tribus, R. Kaindl, *Inorg. Chem.* **2015**, *54*, 6836–6848.

[13] D. Tuschel, *Spectroscopy (Santa Monica)* **2017**, *32*, 13–18 and 24.

[14] K. McGuire, N. D. Lowhorn, T. M. Tritt, A. M. Rao, *J. Appl. Phys.* **2002**, *92*, 2524–2527.

[15] a) A. P. Shpak, A. M. Korduban, M. M. Medvedskij, V. O. Kandyba, *J. Electron Spectrosc. Relat. Phenom.* **2007**, *156–158*, 172–175; b) R. Ji, D. Zheng, C. Zhou, J. Cheng, J. Yu, L. Li, *Materials* **2017**, *10*, 820; c) M. Tong, G. Dai, D. Gao, *Mater. Chem. Phys.* **2001**, *69*, 176–179; d) L. Yan, J. Shu, C. Li, X. Cheng, H. Zhu, H. Yu, C. Zhang, Y. Zheng, Y. Xie, Z. Guo, *Energy Storage Mater.* **2019**, *16*, 535–544.

[16] Z. Jian, X. Lu, Z. Fang, Y.-S. Hu, J. Zhou, W. Chen, L. Chen, *Electrochem. Commun.* **2011**, *13*, 1127–1130.

[17] a) G. Huang, P. Guo, J. Wang, S. Chen, J. Liang, R. Tao, S. Tang, X. Zhang, S. Cheng, Y.-C. Cao, S. Dai, *Chem. Eng. J.* **2020**, *384*, 123313; b) C. Guo, Y. Guo, R. Tao, X. Liao, K. Du, H. Zou, W. Zhang, J. Liang, D. Wang, X.-G. Sun, S.-Y. Lu, *Nano Energy* **2022**, *96*, 107121; c) C. Guo, K. Du, R. Tao, Y. Guo, S. Yao, J. Wang, D. Wang, J. Liang, S.-Y. Lu, *Adv. Funct. Mater.* **2023**, 2301111.

[18] a) L. Fei, Y. Xu, X. Wu, Y. Li, P. Xie, S. Deng, S. Smirnov, H. Luo, *Nanoscale* **2013**, *5*, 11102–11107; b) Q. Cheng, J. Liang, N. Lin, C. Guo, Y. Zhu, Y. Qian, *Electrochim. Acta* **2015**, *176*, 456–462; c) J. Shen, H. Wang, Y. Zhou, N. Ye, G. Li, L. Wang, *RSC Adv.* **2012**, *2*, 9173–9178.

[19] G. Huang, S. Chen, P. Guo, R. Tao, K. Jie, B. Liu, X. Zhang, J. Liang, Y.-C. Cao, *Chem. Eng. J.* **2020**, *395*, 125122.

[20] R. Muruganantham, M.-C. Lin, P. K. Wang, B. K. Chang, W.-R. Liu, *J. Taiwan Inst. Chem. Eng.* **2022**, *131*, 104187.

[21] Y. Yang, H. Zhu, J. Xiao, H. Geng, Y. Zhang, J. Zhao, G. Li, X.-L. Wang, C. C. Li, Q. Liu, *Adv. Mater.* **2020**, *32*, 1905295.

[22] K. Tian, Z. Wang, H. Di, H. Wang, Z. Zhang, S. Zhang, R. Wang, L. Zhang, C. Wang, L. Yin, *ACS Appl. Mater. Interfaces* **2022**, *14*, 10478–10488.

[23] X. Lu, Z. Jian, Z. Fang, L. Gu, Y.-S. Hu, W. Chen, Z. Wang, L. Chen, *Energy Environ. Sci.* **2011**, *4*, 2638–2644.

[24] R. Inada, R. Kumasaka, S. Inabe, T. Tojo, Y. Sakurai, *J. Electrochem. Soc.* **2019**, *166*, A5157-A5162.

[25] M. Si, D. Wang, R. Zhao, D. Pan, C. Zhang, C. Yu, X. Lu, H. Zhao, Y. Bai, *Adv. Sci.* **2020**, *7*, 1902538.

[26] K. Liu, J.-a. Wang, J. Yang, D. Zhao, P. Chen, J. Man, X. Yu, Z. Wen, J. Sun, *Chem. Eng. J.* **2021**, *407*, 127190.

[27] H. Lindström, S. Södergren, A. Solbrand, H. Rensmo, J. Hjelm, A. Hagfeldt, S.-E. Lindquist, *J. Phys. Chem. B* **1997**, *101*, 7717–7722.

[28] a) R. Qian, R. Yao, F. Xiao, T. Yao, H. Lu, Y. Liu, J.-W. Shi, Y. Cheng, H. Wang, *J. Colloid Interface Sci.* **2022**, *608*, 1782–1791; b) R. Qian, H. Lu, T. Yao, F. Xiao, J.-W. Shi, Y. Cheng, H. Wang, *ACS Sustainable Chem. Eng.* **2022**, *10*, 61–70.

[29] K. J. Griffith, I. D. Seymour, M. A. Hope, M. M. Butala, L. K. Lamontagne, M. B. Preefer, C. P. Koçer, G. Henkelman, A. J. Morris, M. J. Cliffe, S. E. Dutton, C. P. Grey, *J. Am. Chem. Soc.* **2019**, *141*, 16706–16725.

[30] a) Y.-S. Hsiao, C.-W. Chang-Jian, H. Chu Weng, H.-H. Chiang, C.-Z. Lu, W. Kong Pang, V. K. Peterson, X.-C. Jiang, P.-I. Wu, C.-P. Chen, J.-H. Huang, *Appl. Surf. Sci.* **2022**, *573*, 151517; b) C. Yu, Y. Bai, D. Yan, X. Li, W. Zhang, *J. Solid State Electrochem.* **2014**, *18*, 1933–1940; c) N. Wan, T. Zhao, S. Sun, Q. Wu, Y. Bai, *Electrochim. Acta* **2014**, *143*, 257–264.

[31] a) S. Chen, R. Tao, J. Tu, P. Guo, G. Yang, W. Wang, J. Liang, S.-Y. Lu, *Adv. Funct. Mater.* **2021**, *31*, 2101199; b) J. Liang, Z. Wang, L. Huang, P. Zou, X. Liu, Q. Ni, X. Wang, W. Wang, R. Tao, *ACS Mater. Lett.* **2023**, 944–954.

[32] Y. Yang, H. Zhu, F. Yang, F. Yang, D. Chen, Z. Wen, D. Wu, M. Ye, Y. Zhang, J. Zhao, Q. Liu, X. Lu, M. Gu, C. C. Li, W. He, *Nano Lett.* **2021**, *21*, 9675–9683.